Int J Appl Earth Obs Geoinformation 64 (2018) 237–248

Contents lists available at ScienceDirect

Int J Appl Earth Obs Geoinformation

journal homepage: www.elsevier.com/locate/jag

Research Paper

Wavelength feature mapping as a proxy to mineral chemistry for investigating geologic systems: An example from the Rodalquilar epithermal system

Freek van der Meer[a,*], Veronika Kopačková[b], Lucie Koucká[b], Harald M.A. van der Werff[a], Frank J.A. van Ruitenbeek[a], Wim H. Bakker[a]

[a] University of Twente, Faculty of Geo-information Science and Earth Observation, Department of Earth Systems Analysis, Hengelosestraat 99, 7514 AE Enschede, The Netherlands
[b] Czech Geological Survey, Klárov 3, Prague 1, 118 21, Czech Republic

ARTICLE INFO

Keywords:
Wavelength mapping
Absorption features
Geology
Hyperspectral imaging
HyMAP
Rodalquilar
SE Spain

ABSTRACT

The final product of a geologic remote sensing data analysis using multi spectral and hyperspectral images is a mineral (abundance) map. Multispectral data, such as ASTER, Landsat, SPOT, Sentinel-2, typically allow to determine qualitative estimates of what minerals are in a pixel, while hyperspectral data allow to quantify this. As input to most image classification or spectral processing approach, endmembers are required. An alternative approach to classification is to derive absorption feature characteristics such as the wavelength position of the deepest absorption, depth of the absorption and symmetry of the absorption feature from hyperspectral data. Two approaches are presented, tested and compared in this paper: the 'Wavelength Mapper' and the 'QuanTools'. Although these algorithms use a different mathematical solution to derive absorption feature wavelength and depth, and use different image post-processing, the results are consistent, comparable and reproducible. The wavelength images can be directly linked to mineral type and abundance, but more importantly also to mineral chemical composition and subtle changes thereof. This in turn allows to interpret hyperspectral data in terms of mineral chemistry changes which is a proxy to pressure-temperature of formation of minerals. We show the case of the Rodalquilar epithermal system of the southern Spanish Gabo de Gata volcanic area using HyMAP airborne hyperspectral images.

1. Introduction

High spectral resolution (hyperspectral) remote sensing data has proven its value since the advent of imaging spectrometer systems in the early 1980's (Abrams et al., 1977). In various earth science application domains hyperspectral data are readily used for example in hydrology to study water quality (Brando and Dekker, 2003), in leaf biochemistry (Kokaly and Clark, 1999; Youngentob et al., 2012) and in geology. Geologic remote sensing scientists have been founding hyperspectral imaging and it can be concluded that the mineral industry and to a lesser extent the oil and gas industries (Kokaly et al., 2013; Lammoglia and de Souza, 2011) use hyperspectral data for exploration. Hyperspectral imaging is also used in practice outside the realm of earth or geosciences for example in art to study paintings (Capobianco et al., 2015; da Silva et al., 2015), the pharmaceutical industry uses it for quality control (da Silva et al., 2015; Mainali et al., 2014) and hyperspectral scanners are used for medical imaging (Calin et al., 2014; Lu and Fei, 2014). In earth sciences, hyperspectral imaging is conducted at various scales varying from rock samples (Cooper et al., 2002; Green and Schodlok, 2016) through core scanning (Bolin and Moon, 2003; Mathieu et al., 2017; Tappert et al., 2015) and outcrop scanning (Buckley et al., 2013; Kurz and Buckley, 2016; Murphy et al., 2012; Snyder et al., 2016) to airborne and space borne acquisition (van der Meer et al., 2012). There are several airborne hyperspectral imaging systems that are operated on a commercial basis and recently also drones have been used for geologic remote sensing (Jakob et al., 2017). The advent of the commercial worldview-3 satellite that has a number of high spectral resolution bands in the shortwave infrared that allow mapping of alteration minerals has resulted in a number of interesting publications (Asadzadeh and de Souza, 2016a; Grebby et al., 2014; Kruse and Perry, 2013). At present, there are two operational spaceborne hyperspectral systems: NASA's Hyperion (Pearlman et al., 2003)

* Corresponding author.
E-mail addresses: f.d.vandermeer@utwente.nl (F. van der Meer), veronika.kopackova@seznam.cz (V. Kopačková), lucie.koucka@geology.cz (L. Koucká), harald.vanderwerff@utwente.nl (H.M.A. van der Werff), f.j.a.vanruitenbeek@utwente.nl (F.J.A. van Ruitenbeek), w.h.bakker@utwente.nl (W.H. Bakker).

http://dx.doi.org/10.1016/j.jag.2017.09.008
Received 24 July 2017; Received in revised form 18 September 2017; Accepted 21 September 2017
Available online 30 September 2017
0303-2434/

on the EO-1 (no longer operational) and ESA's Compact High Resolution Imaging Spectrometer on the Proba-1 (Barnsley et al., 2004). Several spaceborne hyperspectral instruments never reached the design stage, starting with NASA's High Resolution Imaging Spectrometer (HIRISE) and the Australian Resource Information and Environment Satellite (ARIES) in the early 1990's to more recent initiatives such as the Process Research by an Imaging Space Mission (PRISM) from ESA, the Hyperspectral Environment and Resource Observer (HERO) from the Canadian Space Agency (CSA), and the Hyperspectral Earth Observer (HypSEO) from the Italian Space Agency (ASI) (Buckingham and Staenz, 2008; Staenz and Held, 2012). A spaceborne hyperspectral instrument that is going to fly is the German EnMAP system (Stuffler et al., 2007).

The final products stemming from hyperspectral image analysis in geology typically are mineral maps characterizing the earth surface. Many studies have focused on mineral mapping of ore forming mineral systems (see for an overview for example (Goetz, 2009)). Mineral mapping requires so-called endmember spectra that serve as input to a hard classification or a mixture modeling analysis. There are several automated techniques proposed to derive these endmember from hyperspectral data cubes such as the N-FiNDR (Winter, 1999; Zortea and Plaza, 2009), simplex growing algorithms (Chang et al., 2010) and the pixel purity index (PPI) embedded in the ENVI® software (Boardman, 1994).

To arrive at a mineral map, hard classifiers or mixture modeling are the most popular approaches in geologic remote sensing (Kumar et al., 2010). The spectral angle mapper (Kruse et al., 1993), which calculates the angle between two vectors resulting from endmember spectra and pixel spectra, is often used (Bishop et al., 2011; Tangestani et al., 2008). Alternatively, mixture modeling using spectral unmixing techniques (Keshava and Mustard, 2002; Settle and Drake, 1993) is used to arrive at abundances of the various endmembers per pixel (Bedini, 2009; Ferrier et al., 2002; Kruse, 2015; Neville et al., 2003; Notesco et al., 2014; van der Meer, 1996). A comprehensive overview of spectral matching techniques used by the geologic remote sensing community is found in (Asadzadeh and de Souza, 2016b). Mineral maps have been and will be the backbone of any geologic study based on hyperspectral data. However hyperspectral data inherently contain additional spectral information that can be a proxy for mineral chemistry and crystallinity which can be related to metamorphic grade and can enhance our understanding of geologic processes when studying hydrothermal systems.

In this paper we present and compare two approaches that allow to single out endmember spectra in a reproducible, repeatable and transferable manner: 'QuanTools' (Kopacková, 2015; Kopacková and Koucká, 2014a,b) and 'Wavelength Mapper' (Bakker et al., 2011). Both methods produce absorption feature wavelength and depth products from hyperspectral image data. 'QuanTools' uses this information to obtain endmembers for crisp and hard classified mineral maps while the 'Wavelength Mapper' (van Ruitenbeek et al., 2014) produces a soft classification product by merging absorption position and depth into a hue/brightness image that can be interpreted in terms of material properties. The paper intends to compare the two methods and also point out which processing strategy is better under which environmental conditions and we discuss how this can enhance our understanding of the information content of hyperspectral data going from mineral classes to mineral chemistry data. We use HyMAP airborne hyperspectral data from the Rodalquilar mining area in south eastern Spain; a 'Cuprite-like' classic sensor calibration site in Europe and produce an geologic interpretation of the system based on HyMAP airborne hyperspectral mineral and wavelength maps.

The aim of this study is (1) to show two independent and repeatable approaches ('Quantools' and the 'Wavelength Mapper') to derive mineral information based on absorption feature parameters, (2) to illustrate how these approaches do not require endmembers, (3) to compare the results of these two methods, and (4) to apply them to mapping of an epithermal system.

2. Study area and data sets

2.1. The Rodalquilar epithermal system; study area

The study area is located in south eastern Spain in the Gabo de Gata volcanic belt (Fig. 1) which is primarily composed of andesites and rhyolites host rocks overlain by a younger reef complex. These units were formed by late staged Tertiary volcanism giving rise to extensive alteration of the volcanic host rock. Path finder minerals for high sulphidation copper-gold deposits in the area are vuggy quartz, alunite, kaolinite, montmorillonite and chlorite. Silicic, advanced argillic, intermediate argillic and propylitic alteration assemblages have been mapped using field geologic investigation approaches, the area has been extensively studied by geochemist to unravel the mineralization history (Arribas et al., 1995; Rytuba et al., 1990). There are a number of geologic remote sensing studies conducted in the Rodalquilar area (using HyMAP airborne hyperspectral data and ASTER data) that report mineral maps as a proxy to the ore at local or regional scale (Bedini et al., 2009; Carranza et al., 2008; Debba et al., 2009, 2006; Ferrier et al., 2009; Ferrier and Wadge, 1996; Mielke et al., 2016; van der Meer, 2006; van der Werff and van der Meer, 2015).

2.2. HyMAP airborne hyperspectral data

In this study we use airborne hyperspectral data from the HyMAP airborne hyperspectral sensor manufactured by Integrated Spectronics and for our flight campaign (May 18, 2004) operated by the German Aerospace Center (DLR). HyMap has a total of 128 spectral bands in 4 modules (of 32 bands each), covering the visible 0.45–0.89 μm wavelength range at 15 nm spectral sampling intervals, near infrared 0.89–1.35 μm wavelength range at 15 nm spectral sampling intervals, and two modules in the shortwave infrared SWIR 1 1.40–1.80 μm wavelength range at 13 nm spectral sampling intervals and SWIR 2 1.95–2.48 μm wavelength range at 17 nm spectral sampling intervals. Pre-processing to reflectance-at-surface (at 4 m nominal ground resolution) was done by DLR using ATCOR (ATmospheric CORrection) 4 (Richter and Schlapfer, 2002) and geometric correction was done with PARGE (Schlapfer and Richter, 2002).

3. Spectral absorption mapping methods and results

In this section we give a technical description of the two tools we use and compare to spectrally map absorption feature characteristics: 'QuanTools' and the 'Wavelength mapper'. Next, we discuss endmember selection and finally we present results which are compared and interpreted in the discussion section.

3.1. 'QuanTools' (Kopacková, 2015; Kopacková and Koucká, 2014a,b)

'QuanTools' (see Fig. 2 for the processing steps) is a technique that derives spectral absorption band parameters from reflectance spectral data using either spectral libraries or hyperspectral images. First step is a continuum removal (Clark and Roush, 1984) by which the continuum that is a convex hull of straight-line segments is fitted over a reflectance spectrum and subsequently removed by division or rationing. The second step is a noise detection and removal. This step uses local minima of the spectral curve defined as:

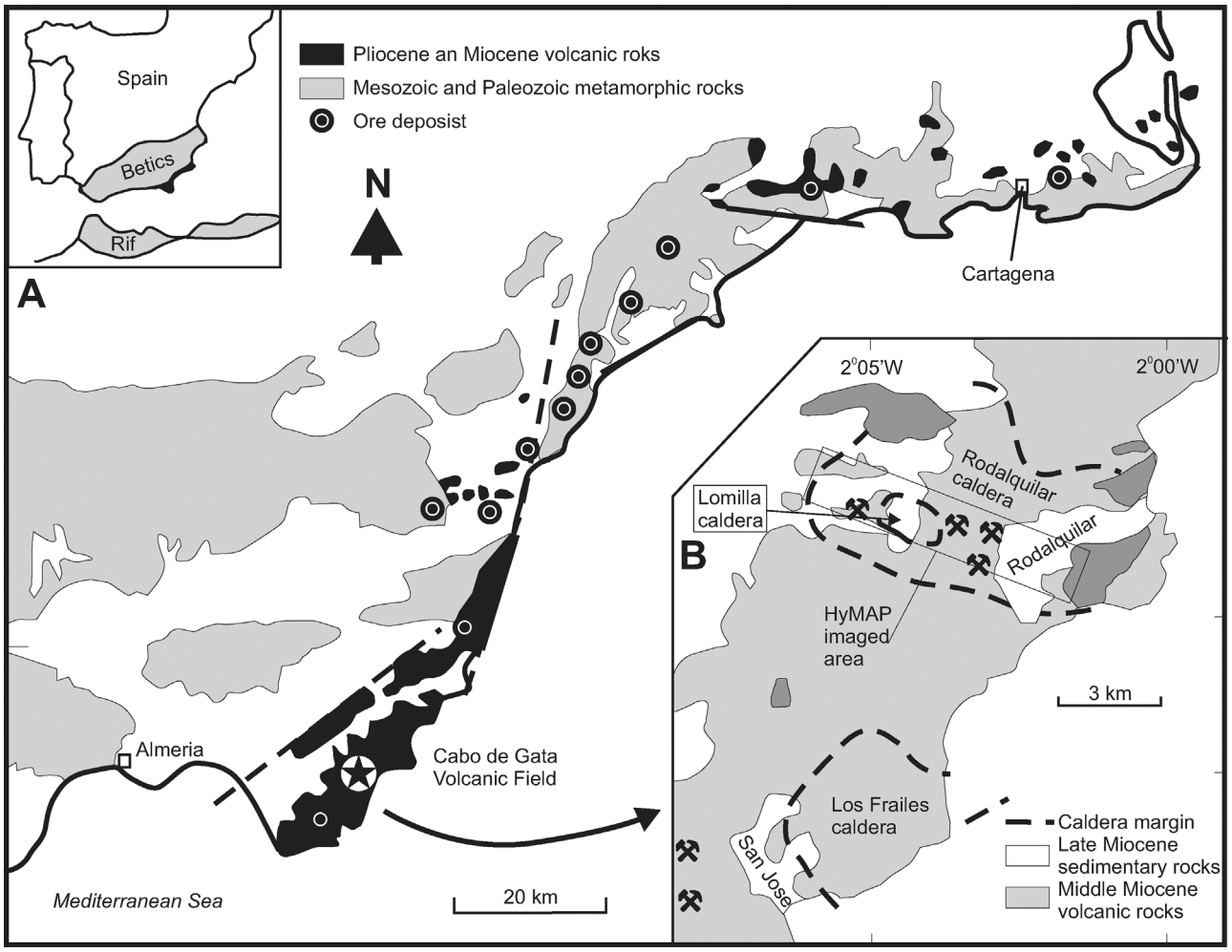

Fig. 1. Location of the study area (the Rodalquilar gold mining area in the Gabo de Gata volcanic belt of south eastern Spain). Geologic map modified after Arribas et al. (1995).

$$R = \begin{Bmatrix} 1\ if \rho_{CR}(\lambda - 1) \geq \rho_{CR}(\lambda) \\ 0\ if \rho_{CR}(\lambda - 1) < \rho_{CR}(\lambda) \end{Bmatrix}$$

$$if\ \ [R(\lambda - 1) = 1] \wedge [R(\lambda) = 0] \Rightarrow localminimum \tag{1}$$

where $\rho_{CR}(\lambda)$ and $\rho_{CR}(\lambda - 1)$ are saddle (or shoulder) values of local minima from the continuum removed data. The method calculates local minima along the spectral curve and determines a minimum absorption feature depth threshold for an absorption feature to be considered instrument noise or a real absorption feature that can be related to mineralogy or chemical variations. For this two lowest values $A_{min}(\lambda)$ and $B_{min}(\lambda)$, calculated from the bands placed before and after the local minimum within the set spectral window, are compared to the local minimum $\rho_{CR}(\lambda)$ and are used to detect the noise:

$$[B_{\min}(\lambda) < \rho_{CR}(\lambda)] \wedge [A_{\min}(\lambda) > \rho_{CR}(\lambda)]: \Rightarrow printErr(\lambda) \tag{2}$$

After a noise cleaned image (see Fig. 3 for an example) is retained the next step is to derive the actual absorption features and their parameters (e.g., wavelength position and depth) using the continuum depth of a feature:

$$CRdepth(\lambda) = 1 - \rho_{CR}(\lambda) \tag{3}$$

Using trend analysis first the saddle points or shoulders of each absorption feature are detected as local absorption maxima satisfying the condition:

$$R_{ij} = \begin{Bmatrix} 1 if CRdepth(\lambda)_{ij} \geq CRdepth(\lambda - 1)_{ij} \\ 0 if CRdepth(\lambda)_{ij} < CRdepth(\lambda - 1)_{ij} \end{Bmatrix} \tag{4}$$

Whilst only if the following conditions applies:

$$if\ \ [R(\lambda - 1)_{i,j} = 1] \wedge [R(\lambda)_{i,j} = 0] \Rightarrow print\ Loc\_\max_{ij} \tag{5}$$

Next the absorption feature position and depth is calculated using the bands in between the saddles. The algorithm allows the user to select the number of absorption features that the user wants to detect for a certain wavelength range. This is a condensed outline of the algorithm, a more elaborate mathematical formulation of the algorithm is found in this paper that is under review while we write (Kopačková and Koucká, 2017).

3.2. 'Wavelength Mapper' (Bakker et al., 2011; van Ruitenbeek et al., 2014)

The 'Wavelength Mapper' (Bakker et al., 2011) is an semi-automatic approach to estimating the position of the deepest absorption and the associated wavelength of a spectral absorption feature of a mineral. The 'Wavelength Mapper' (Bakker et al., 2011) first requires the user to set a wavelength region of interest for which the convex Hull is calculated and removed by division to obtain continuum removed spectra (Clark

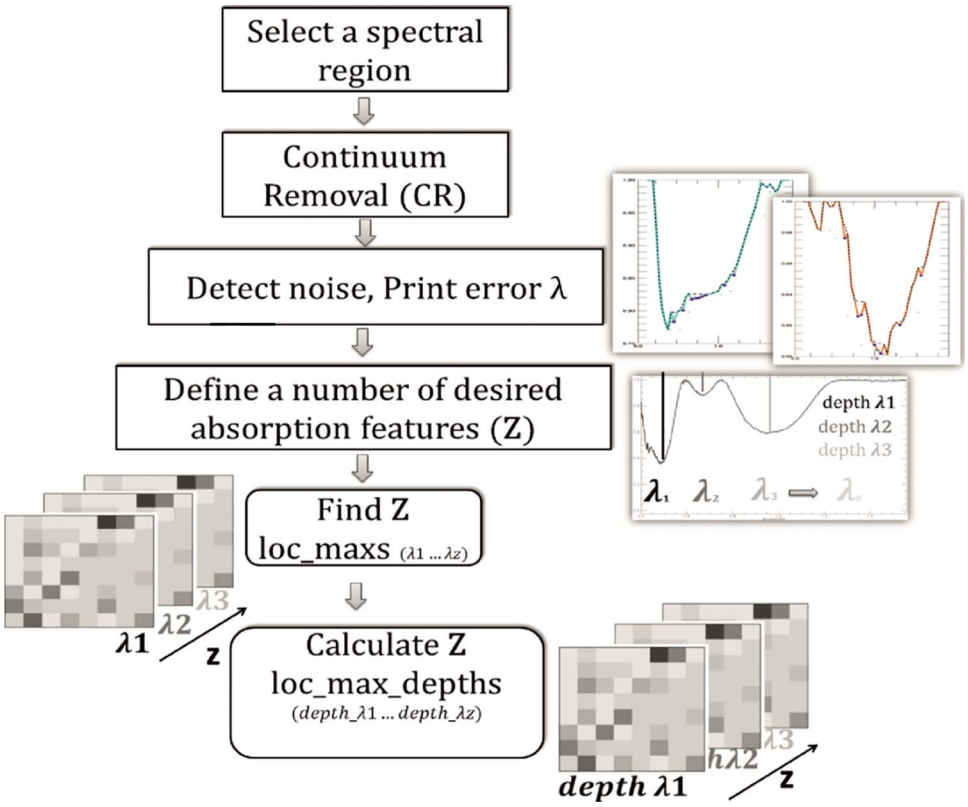

Fig. 2. A simplified processing scheme for the 'QuanTools' (CR: continuum removal, λ: wavelength, loc_mac: local absorption feature maximum, loc_max_depth: absorption feature depth).

and Roush, 1984). Next the wavelength position of the deepest absorption feature per pixel and per wavelength region are derived following (Rodger et al., 2012) and a second order parabolic fit as follows (see Fig. 4 for a graphical example):

$$w(x) = ax^2 + bx + c \quad (6)$$

Where $w(x)$ is the interpolated value at wavelength position x and a, b, c are the coefficient of the parabolic function. The interpolated position at the minimum reflectance w_{min} as a function of the coefficients of the parabola a, b is:

$$w_{min} = \frac{-b}{2a} \quad (7)$$

and the absorption depth is given as:

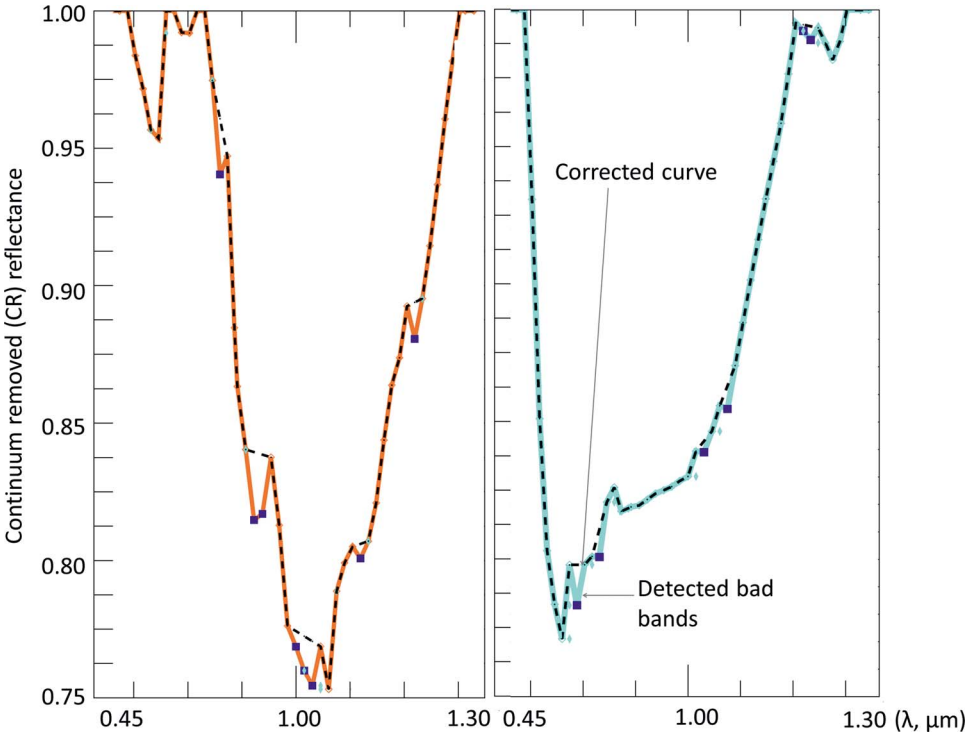

Fig. 3. Bad band detection in 'QuanTools' where the detected bad bands are shown by the blue square points and the corrected curve as a dashed line (set spectral window: 3 neighboring bands). (For interpretation of the references to color in this figure legend, the reader is referred to the web version of this article.)

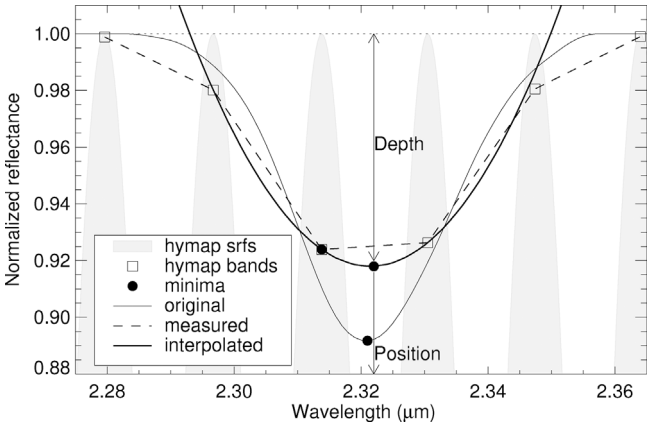

Fig. 4. The wavelength mapper fits a parabola through three consecutive image points to arrive at the exact position and depth of an absorption feature modified after van Ruitenbeek et al. (2014).

$$depth = 1 - f(w_{\min}) \quad (8)$$

The resulting product is two images which for each pixel in the original HyMAP image give (1) the interpolated wavelength position of the deepest absorption feature and (2) the depth of this absorption feature relative to the Hull. These two images are combined into a single image product by a HSV to RGB transformation where the Hue is obtained from the wavelength position, and the Value is obtained from the depth of the absorption feature.

3.3. Results and comparison of the two wavelength mapping methods

We compared the mapped absorption feature characteristics of 'QuanTools' (Fig. 5) and 'Wavelength Mapper' (Fig. 6) for the 3 major absorption features mapped in the VNIR and SWIR, respectively. The 'Wavelength Mapper' assigns the absorption wavelength positions to a new multi-band raster ordered given by consecutive absorption depths while the 'QuanTools' assigns the absorption wavelength positions ordered from shorter to longer wavelengths. This is a difference between the two compared approaches. Each absorption feature mapped at distinct wavelength position can be characterized by variable absorption depths. As a result the 'Wavelength Mapper' can assign the same absorption wavelengths in different band-orders depending on how corresponding absorption depths are sorted when compared to one another. On the other hand, 'QuanTools' always places the absorption features mapped at distinct wavelength positions, although present with variable absorption depths, in the same way as the wavelengths themselves determine the band order. Therefore, even in a case that the 3 major absorption features over the VNIR and SWIR regions were mapped identically using both approaches, we got 6 possible different combinations (P(3) = 3!) for the 'Wavelength Mapper' compared to the only 1 combination possible for the 'QuanTools'. A verification that wavelength positions was therefore not straightforward, and could not be demonstrated using simple scatterplots between the corresponding 'Wavelength Mapper' and 'QuanTools' wavelength bands as demonstrated in Fig. 7. For instance, scatterplots show that in both the VNIR and SWIR regions the first absorption features assigned by either approach (VNIR: WL_B1_ITC vs. WL_B1_CGS, SWIR: WL_B4_ITC vs. WL_B4_CGS) were only in a few cases placed at the shortest wavelengths and at the same time were also the most pronounced ones.

Table 1 shows the wavelength mapping using the whole image statistics on the detected wavelength positions (3 major in VNIR and 3 major in the SWIR). It shows that 'QuanTools' and the 'Wavelength Mapper' produce similar absorption features. Comparing the absorption wavelength mapping for four selected targets, the same absorption wavelength maxima were detected using both approaches, however the band order they were assigned to is different (see Table 2). This is the result of the different ordering of results as discussed above.

In addition, we used the matrices projecting all together the combinations among the three major absorption wavelength positions that were mapped in the VNIR (Fig. 8) and SWIR (Fig. 9) by the 'Wavelength Mapper' (P(3) = 3! combinations) and 'QuanTools' (only 1 combination). The statistics is based on 28 different region of interest (ROIs) totaling 13 366 pixels collected for different surface targets. As already described, using the two approaches the order of absorption wavelength positions is assigned into multi-band wavelength rasters in different band-orders. Fig. 8A shows a matrix where all 3 major absorptions mapped by the 'Wavelength Mapper' within the VNIR region are projected in all possible wavelength band-orders. Similarly, Fig. 9A shows the same for the 3 major absorptions mapped within the SWIR region. The Figs. 8A and 9A then demonstrate a case when the matrix must be 100% diagonally symmetric as all mapped absorption features, respectively their wavelengths, are projected in all possible band combinations. On the other hand, Figs. 8B and 9B then show matrices where are projected only the real combinations found for the 3 major absorptions mapped by the 'Wavelength Mapper' and the 'QuanTools' within the VNIR and SWIR region, respectively. In a case, that both approaches detect the absorption wavelengths identically, although assigned in different band-orders, the matrices have to be also diagonally symmetric.

The level of diagonal symmetry can be then used to assess the absorption wavelength mapping results, respectively if both approaches detected the absorption wavelength positions identically. We can infer from Fig. 8B some minor deviations from 100% symmetry meaning that in some cases the actual position mapped by 'QuanTools' was shifted by a fraction in the order of 0.01 μm to shorter wavelength which we attribute to the fact that the 'wavelength mapper' uses a parabolic fit over 3 consecutive bands in a spectrum. Fig. 9B shows the same results but mapped in the SWIR region. It can be seen that the 'Wavelength Mapper' versus 'QuanTools' matrices are (again) nearly symmetric (no smoothing was used for the SWIR bands when using 'QuanTools').

The resulting wavelength maps produced by 'Quantools' and the 'Wavelength mapper' compare favorably in shape and outline to mineral maps published earlier for the Rodalquilar area using the same HyMAP data set (Bedini et al., 2009; Mielke et al., 2016). In the next section we provide an interpretation of the wavelength position and depth information in relation to a better understanding of the alteration patterns that can be depicted in the Rodalquilar area. We decided to show the true merit of this information in understanding hydrothermal systems rather than going into an absolute validation of the image data products using a confusion matrix approach and Kappa statistics. This is justified by a recent publication by some of the authors originally proposing Kappa-type statistics who now conclude that Kappa indices are misleading and biased (Pontius and Millones, 2011). These authors also seem to suggest that it is of more importance to focus on the actual interpretation of the results. In other words, we are not so worried about the absolute validity of our results or how well they match with the published geologic map (which is also based on sparse field data and human interpretation), but we want to show that our results are reproducible and more important that they show insights into understanding the mineral distribution and subtle geochemical variations of an hydrothermal system.

4. Geologic interpretation and implications for the Rodalquilar epithermal system

Fig. 10 shows the results of absorption feature mapping using both 'quantools' and the 'wavelength mapper' for the northeastern part of the HyMAP scene over the Rodalquilar alteration system. The top part of Fig. 10 shows a transect (indicated on the geologic map in Fig. 10) depicting the wavelength position and depth as mapped by the two

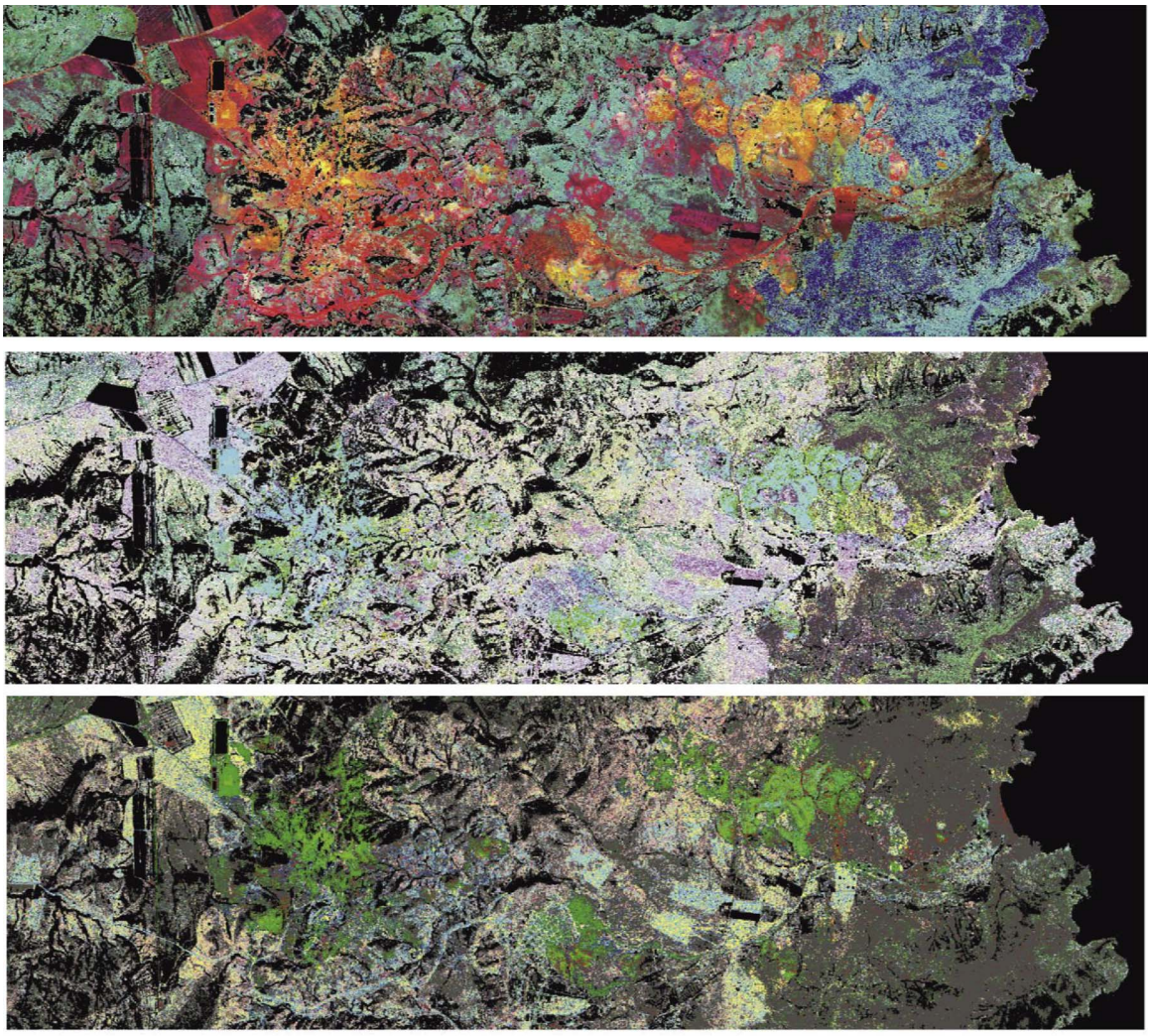

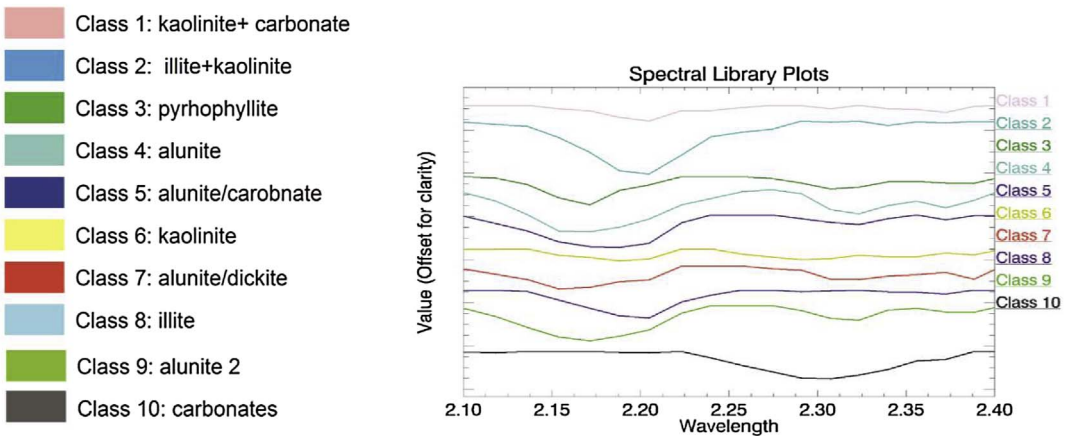

Fig. 5. The results of absorption mapping using 'QuanTools'. Top: Absorption depths of the 1st, 2nd and 3rd feature, displayed in an RGB color composite. Center: Absorption wavelength positions of the 1st, 2nd and 3rd feature, displayed in an RGB color composite. Wavelengths are ordered from short (2.1 μm) to long (2.4 μm). Bottom: The result of a "hard" classification employed to absorption wavelength raster and representative spectrum of the derived mineral classes.

methods. The geologic map (Arribas, 1993) of the area together with the mineral maps resulting from the two methods is shown at the bottom of Fig. 10.

The area in this part of the system is underlain by two type of ignimbrites (unit 10 and 12), rhyolite and dacite domes (unit 8 and 11), and an andesitic intrusion (unit 14). The igneous lithologies are overlain by a younger reef complex (unit 12). Thin soils have been developed in most lithological units. All lithologies in this area are of Miocene age, except alluvial and colluvium sediments that are of Quaternary age (unit 21). The volcanic lithologies have all been affected by hydrothermal alteration events that are associated with the epithermal mineralization at Rodalquilar (Arribas et al., 1995).

The wavelength map in Fig. 10 shows the variation in surface mineralogy in a variety of different rainbow colors. Outcrops of altered volcanic rocks show in bright cyan to green colors. In these outcrops wavelength positions of deepest absorption features vary between 2160

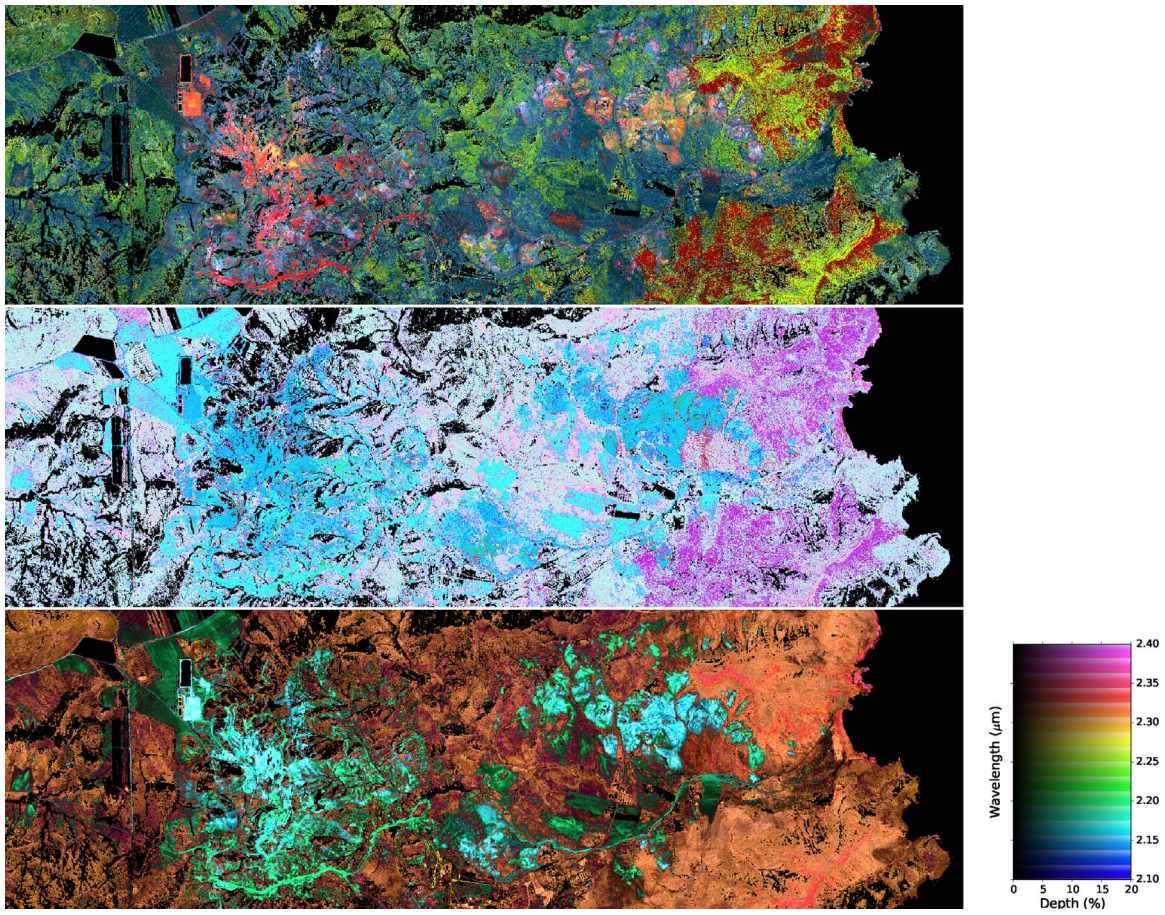

Fig. 6. Result of the absorption feature mapping with the 'wavelength mapper'. Top: Absorption depths of the 1st, 2nd and 3rd feature, displayed in an RGB color composite. Center: Absorption positions of the 1st, 2nd and 3rd feature, displayed in an RGB color composite. Wavelengths are ordered by consecutive absorption depths (from short (2.1 μm) to long (2.4 μm)). Bottom: the wavelength map created by displaying absorption wavelength in a rainbow color ramp and absorption depth in an intensity ramp.

and 2208 nm as can be seen from the wavelength position cross section in Fig. 10. These values are indicative of argillic and advance argillic alteration minerals, such as illite, kaolinite, dickite, pyrophyllite and alunite. Outcrop of limestone rocks of the reef complex show in red-colored pixels, contain abundant calcite and have a wavelength position of approximately 2340 nm. Soil cover is presented in orange colors, which are dispersed through the image and occur in all lithologies. The soils in the area have absorption wavelengths at approximately 2310 nm and contain Mg-clays, Al-clays and calcareous material.

The cluster of hydrothermally altered rock outcrops in this area represents one of the alteration centers in the Rodalquilar hydrothermal system. Hydrothermal fluids have intensely altered the ignimbrite units,

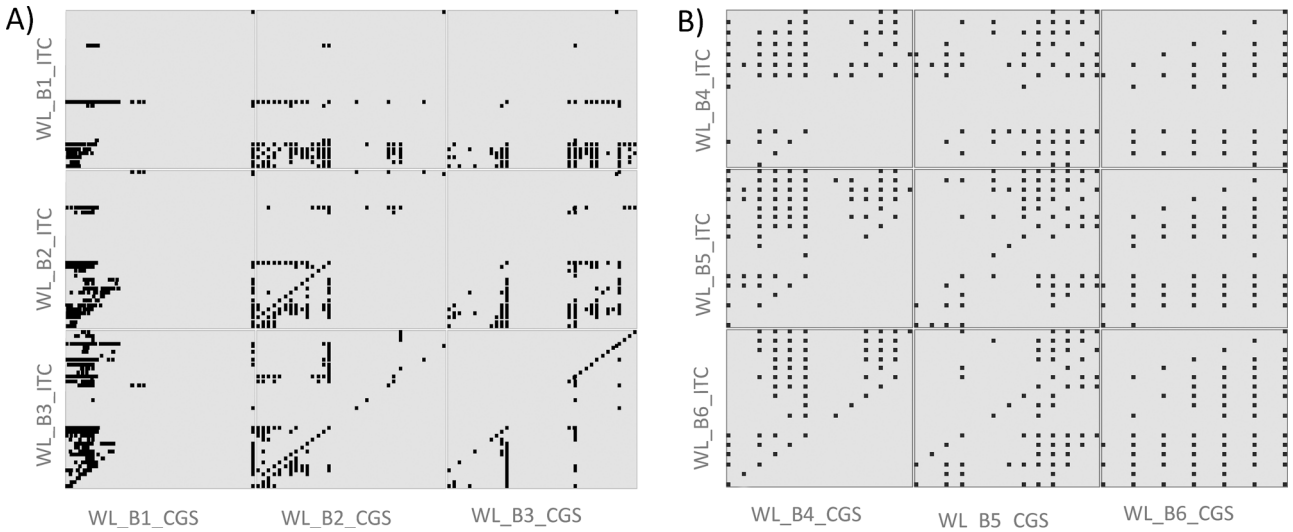

Fig. 7. Scatterplots between the corresponding 'Wavelength Mapper' (ITC) and 'QuanTools' (CGS) wavelength (WL) bands. The statistics is based on 28 different region of interest (ROIs) totaling 13 366 pixels collected for different surface targets. A) Three major absorptions mapped in the VNIR region were assigned into 3 absorptions wavelength bands: B1, B2, B3. B) Three major absorptions mapped in the SWIR region were assigned into 3 absorptions wavelength bands: B4, B5, B6.

Table 1
Wavelength mapping: the whole image statistics on the detected wavelength positions (3 major in VNIR and 3 major in the SWIR).

		QuanTools (CGS)				Wavelength Mapper (ITC)			
		Min	Max	Mean	Stdev	Min	Max	Mean	Stdev
VNIR	1st	0.451700	0.943800	0.502991	0.033955	0.451700	1.038200	0.606620	0.095378
VNIR	2nd	0.000000	1.053600	0.644509	0.076845	0.000000	1.038200	0.568946	0.108891
VNIR	3rd	0.000000	1.053600	0.874405	0.142515	0.000000	1.053600	0.850254	0.172346
SWIR	1st	2.118500	2.323500	2.193940	0.049614	2.118500	2.388400	2.280392	0.058445
SWIR	2nd	0.000000	2.388400	2.295321	0.043023	0.000000	2.388400	2.312362	0.069188
SWIR	3rd	0.000000	2.388400	2.324940	0.268511	0.000000	2.388400	2.217364	0.276503

Table 2
Absorption wavelength mapping: an example for selected 4 targets, the same absorption wavelength maxima were detected using both approaches, however the band order they were assigned to is different.

ROIs		QuanTools (CGS)	Wavelength Mapper (ITC)
VNIR	1st	0.497100	0.679800
VNIR	2nd	0.679800	0.497100
VNIR	3rd	0.928000	0.928000
SWIR	1st	2.153900	2.307400
SWIR	2nd	2.188200	2.188200
SWIR	3rd	2.307400	2.153900

that host the majority of the epithermal mineralization in the Rodalquilar area. The andesitic intrusion (unit 14) is less altered, as is apparent from the absence of hydrothermal alteration minerals. This indicates that the intrusion was emplaced after or at late stage in the hydrothermal alteration event.

The most intense advanced argillic alteration occurs in the center of this cluster of altered rock outcrop and contains alunite and pyrophyllite. These advanced argillic alteration zones in cyan are surrounded by intermediate argillic alteration zones in cyan-green colors containing dickite, kaolinite and illite. These zones grade into propylitic alteration zones in green and contain illite and illite-smectite. The advanced argillic zones have been overprinted in places by supergene acid-sulfate weathering, that increased the abundance of alunite and cyan–colored image pixels. The results presented in mineral maps in Fig. 10 show that the zonation of alteration assemblages is gradual and the boundaries between zones are fuzzy at scale of the airborne image. The change in alteration mineralogy away from the alteration center is the result in a gradual decrease in fluid acidity and temperature and is locally influenced by rock permeability and lithological composition.

5. Discussion

The ‘QuanTools’ approach begins knowledge driven as it requires first to set the wavelength range of the interest, identify and correct bad/noisy bands, if presented in the data, and define the desire number of absorption features. The second (classification) part is data driven because the method uses the absorption features (so not endmember spectra) to produce an unsupervised hard classification. For the ‘Wavelength Mapper’ the parabolic fitting to the image spectra and the derivation of absorption position and depth and the generation of a wavelength map are purely data driven while endmember selection (optional and only needed if one wants to create a hard classification) or further analysis is knowledge driven.

Mineral mapping using hyperspectral data often relies on the availability of spectral libraries of target materials which contain pure mineral spectra while in reality imaged pixels are exclusively mixtures. Most endmember finding and location algorithms are subjective to decisions made by expert geologists or require post processing steps on rule images which in turn require parameterization by image interpreters. The ‘Wavelength Mapper’ and ‘QuanTools’ automatically find the deepest absorption features in a user defined (based on knowledge of where in the spectrum certain minerals show absorption features) spectral range using a hyperspectral data set. ‘QuanTools’ uses this position/depth mapping to map material diversity and locate target materials for further spectral classification while the ‘Wavelength Mapper’ converts the absorption position and depth into hue and brightness which allows to link this to material properties. This allows the user to perform endmember selection for mineral mapping in an unbiased way. This is particularly useful if no prior geologic knowledge of an area is available. Using spectral matching approaches to derive the absorption wavelength position and depth as is done by ‘QuanTools’

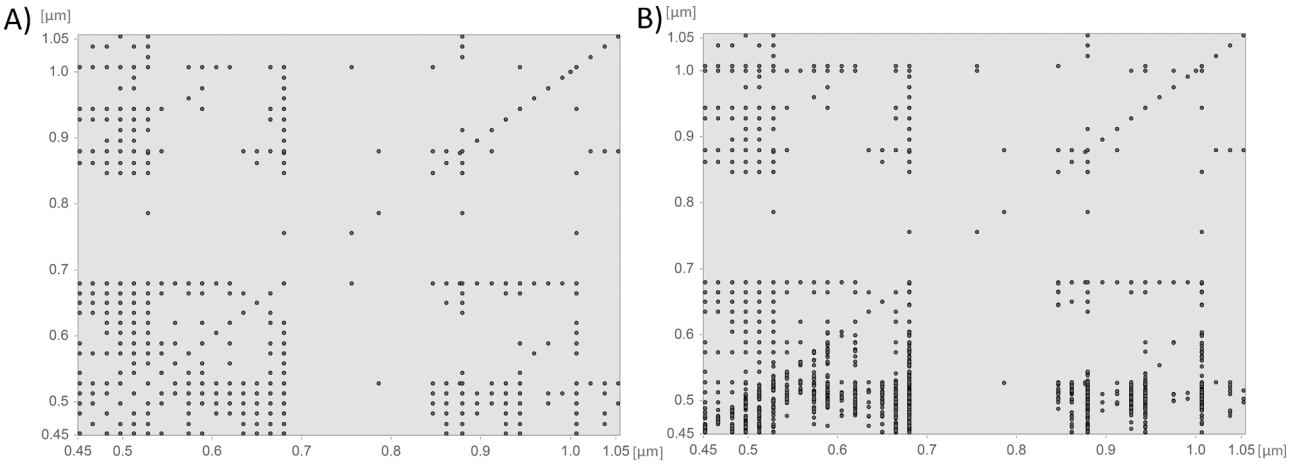

Fig. 8. VNIR region: Matrixes display absorption wavelength mapping results derived from 28 different ROIs collected for different surface targets (28 ROIs, 13 366 pixels). A) A matrix where all 3 major absorptions mapped by the ‘Wavelength Mapper’ are projected in all possible wavelength band-orders. For a comparison, B) shows a matrix where are projected only the real combinations found for the 3 major absorptions mapped by the ‘Wavelength Mapper’ and the ‘QuanTools’.

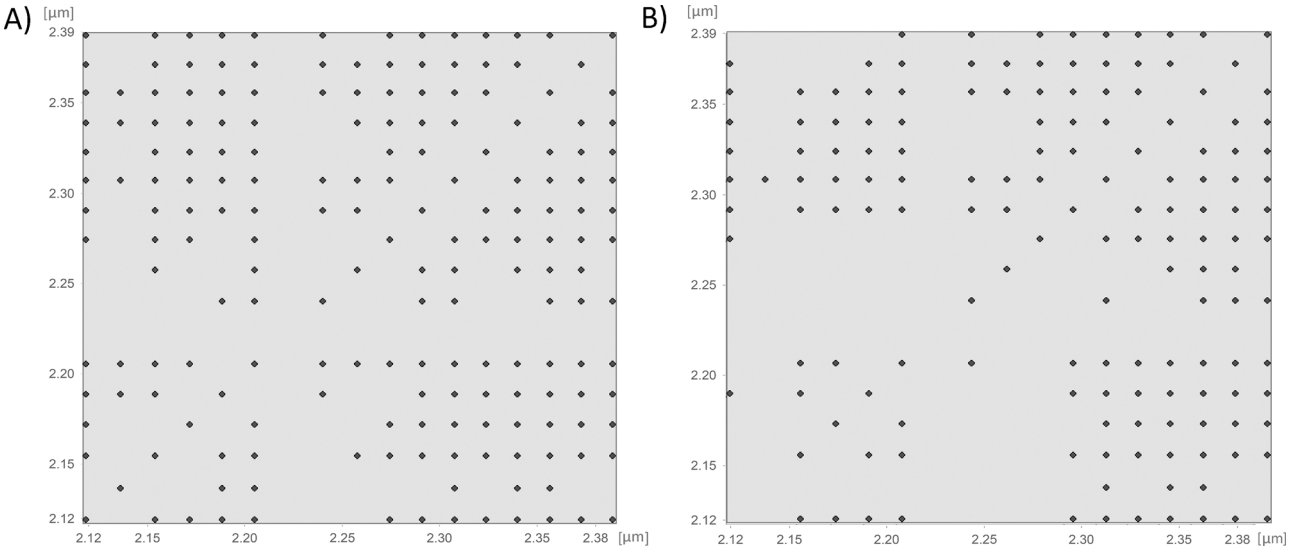

Fig. 9. SWIR region: Matrixes display absorption wavelength mapping results derived from 28 different ROIs collected for different surface targets (28 ROIs, 13 366 pixels). A) A matrix where all 3 major absorptions mapped by the 'Wavelength Mapper' are projected in all possible wavelength band-orders. For a comparison, B) shows a matrix where are projected only the real combinations found for the 3 major absorptions mapped by the 'Wavelength Mapper' and the 'QuanTools'.

and the 'Wavelength Mapper' is reproducible and transferable to other data sets and areas. The 'Wavelength Mapper' allows the user to browse through the image data in both the wavelength position domain as well as the wavelength depth domain or combinations of the two. Assuming the user has the necessary geologic/mineralogic knowledge, the wavelength map allows to look for areas in the image that show diagnostic absorption features that can be related to presence of certain mineral groups.

Hard classification, as obtained with 'QuanTools', brings the spectrum property back to a single map unit and allows consequently deriving a recognized product by the geologic remote sensing community namely the mineral map. However, assigning pixels to mineral classes leads to generalization to some extent. Most (if not all) pixels in an image are mixtures, however assignment to a hard class is based on the most pronounced absorption features representing the dominant mineral. This could cause a loss of information on other (minor) components. On the other hand, 'QuanTools' can offer an easy way to integrate the absorption feature information from optical (0.4-2.5 µm) and thermal (8–14 µm) regions together, thus can allow mapping the mineralogy in more complex way (e.g., iron oxides, phyllosilicates and silicates). This is highly relevant especially in the context of the future satellite missions such as NASA's planned Hyperspectral Infrared Imager (HySpIRI) satellite system, as the way how to integrate the information from optical and thermal hyperspectral data still remains challenging.

Most classifiers, including the Spectral Angle Mapper (SAM) (Kruse et al., 1993), which is a correlation based matching technique and also other correlators like CCSM (van der Meer, 2000) that allows classification when thresholding the rule images, and any form of spectral unmixing, do not explicitly use the depth information of an absorption feature. Depth is a proxy for grain size or scattering volume and may be important in defining the noise limits of a data set; in other words how deep must an absorption feature be for it to be considered data/information instead of instrument noise? Consequently, SAM and unmixing techniques cannot produce seamless maps and require considerable user engagement (Hewson et al., 2005) and intervention (Cudahy, 2016; Cudahy et al., 2010). Wavelength maps are by default seamless map products because they portray the absorption depth and position assuming the sensor has no drift and is stable between different image acquisitions. This is a very important when airborne surveying large areas and stitching together dozens of strips of image data.

By using continuum removal in 'QuanTools' and the 'Wavelength Mapper' these techniques reduce illumination differences (any leftover) shadow effects and differences in scene illumination which has the advantage of enabling the production of seamless map products. However, by doing so, we discard valuable information in the spectra namely the albedo which links to the brightness of an object. The overall reflectance is also a proxy to grain size and other material parameters and more importantly it can be the only handle on mapping of spectrally featureless minerals (such as quartz in the visible to shortwave infrared). Continuum removal method is the only critical issue in the calculation of absorption wavelength depth and position. How this continuum is fitted and is removed from the spectra has a minor but noticeable effect on the position of deepest absorption detected. In both compared approaches, the Continuum removal method described by Clark and Roush (1984) is used, however, recently a new approach for this kind of normalization was suggested (Mielke et al., 2015), in the future it might therefore be interesting to integrate this new method as an alternative into 'QuanTools' and the 'Wavelength Mapper'.

Combined information on the wavelength position and depth can be linked to material chemistry (Van Ruitenbeek et al., 2005). Theoretically it allows to map chemical changes within mineral groups which may be related to such processes as weathering and different stages of alteration and metamorphism. In the SWIR wavelength region, shift in the wavelength position of for example illite, kaolinite or white micas is a proxy for crystallinity which in turn is a proxy for temperature of formation of these minerals are their position in the alteration system. Several studies have reported this for characterization of low-grade metamorphic rocks (Abweny et al., 2016), using illite as a geothermometer in geothermal areas (Battaglia, 2004), using Al-content in muscovite as an indicator for metamorphic grade (Duke, 1994) and using Al-content of white micas to map fluid pathways (Van Ruitenbeek et al., 2005, 2006). Similarly, in the VNIR region, the shift to longer wavelengths of the absorption maximum centered between 0.90 and 1.00 µm is the main parameter that allows differentiation among the ferric minerals (Montero et al., 2005) and has a further potential for Acid Mine Drainage (AMD) mapping (Kopackova, 2014).

Combining surface mineralogy mapping with surface mineral chemistry using subtle variations in absorption feature position and depth can yield geothermometers that allow to mimic hydrothermal processes locating vents, recharge and discharge areas in such systems. Thus surface mineralogy and mineral chemistry information extracted from hyperspectral data provides a synergistic use in the analysis of

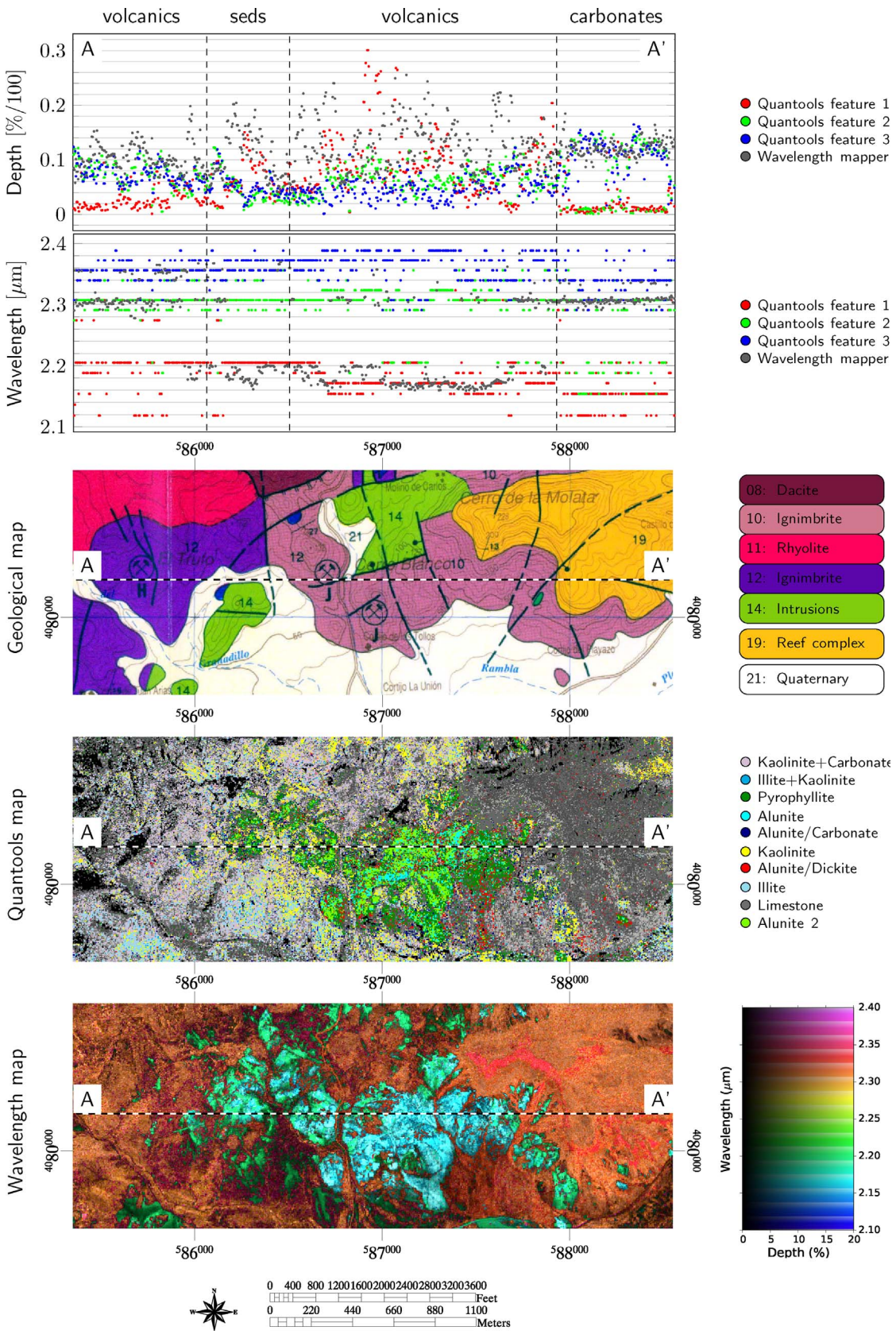

Fig. 10. From top to bottom: results of wavelength position and depth of 'Quantools' and 'wavelength mapping' in the northeastern part of the Rodalquilar hydrothermal system, geological map after Arribas (1993), mineral map constructed with 'Quantools', and mineral map constructed with the 'wavelength mapper'.

hydrothermal systems. When mapping large areas to produce seamless continent-wide material maps, an area in which work has recently started (Cudahy et al., 2010; Hewson et al., 2009), the challenge is to do robust sensor calibration, use physical retrieval models, produce seamless maps that are validated without field data support which physically-based wavelength mapping methods can provide. This is highly relevant especially in a view of the upcoming hyperspectral satellite missions such as EnMap (Stuffler et al., 2007) and HySPIRI (Lee et al., 2015) for geologic studies as discussed in this paper but also for studies on land degradation (Shrestha et al., 2005) and other soil related studies.

6. Conclusions

Two methods are presented in this paper that calculate absorption feature parameters from hyperspectral data: the 'Wavelength Mapper' and the 'QuanTools'. Both methods use a different mathematical solution to deconvolve the hyperspectral data but arrive at the same sets of absorption wavelengths and depths. The algorithms neither require user-dependent settings nor prior definition of endmembers, hence result in 100% reproducible image products.

It can be concluded that although the two methods are based on a different mathematical solution to deconvolve a spectrum into wavelength position of deepest absorption and absorption feature depth they produce comparable results. Furthermore the methods are reproducible and the results are transferable and scalable to other areas and data sets. The absorption feature position is a key variable to link to subtle variations in mineral chemistry (e.g., for example Al-Mg versus OH compositional variation) which in turn can be interpreted in terms of differences in environmental conditions (e.g., fluid composition in case of alteration processes and/or temperatures of the brines). The absorption feature depth is not as straightforward, however it gives us a handle to grain size variation or abundance of certain minerals in a mixture.

We applied both methods to HyMAP airborne hyperspectral data from the Rodalquilar epithermal system and demonstrated how absorption wavelength parameters (depth and position) can be interpreted in terms of subtle changes in mineral chemistry that relates to alteration facies and different stages of volcanism. These subtle wavelength changes are often the result of minor changes in mineral composition which are the result of progressive metamorphism (e.g., changes in the chemical composition of volcanic brines and its temperature). Such wavelength maps can be used as aa geothermometer which gives, when combined with the classical mineral maps gives an unprecedented view on the origin of a hydrothermal system.

Acknowledgements

The 'Wavelength Mapper' is part of the Hyperspectral Python (HypPy) which is a collection of tools that were developed by Wim Bakker at ITC and can be freely downloaded from: https://www.itc.nl/personal/bakker/hyppy.html.

'QuanTools' project was funded by the Ministry of education youth and sports, the Czech Republic (HyperALGO: grant no LH13266) and the toolbox is available for free (February 2016), if interested read more at http://www.cgs-rs.g6.cz/hyperalgo.htmlor contact quantoolscgs@gmail.com.

References

Abrams, M., Ashley, R., Rowan, L.C., Goetz, A.F.H., Kahle, A.B., 1977. Mapping of hydrothermal alteration in the Cuprite mining district, Nevada, using aircraft scanner imagery from 0.46–2.36 micron spectral region. Geology 5, 713–718.

Abweny, M.S., van Ruitenbeek, F.J.A., de Smeth, B., Woldai, T., van der Meer, F.D., Cudahy, T., Zegers, T., Blom, J.K., Thuss, B., 2016. Short-Wavelength Infrared (SWIR) spectroscopy of low-grade metamorphic volcanic rocks of the Pilbara Craton. J. Afr. Earth. Sci. 117, 124–134.

Arribas, A., Cunningham, C.G., Rytuba, J.J., Rye, R.O., Kelly, W.C., Podwysocki, M.H., McKee, E.H., Tosdal, R.M., 1995. Geology, geochronology, fluid inclusions, and isotope geochemistry of the rodalquilar gold alunite deposit, Spain. Econ. Geol. 90 (4), 795–822.

Arribas, A., 1993. Mapa geológico del distrito minero de Rodalquilar. Instituto Tecnólogico GeoMinero de España, Almería.

Asadzadeh, S., de Souza, C.R., 2016a. Investigating the capability of WorldView-3 superspectral data for direct hydrocarbon detection. Remote Sens. Environ. 173, 162–173.

Asadzadeh, S., de Souza, C.R., 2016b. A review on spectral processing methods for geological remote sensing. Int. J. Appl. Earth Obs. Geoinf. 47, 69–90.

Bakker, W.H., van Ruitenbeek, F.J.A., van der Werff, H.M.A., 2011. Hyperspectral image mapping by automatic color coding of absorption features. In: 7th EARSEL Workshop of the Special Interest Group in Imaging Spectroscopy. Edinburgh, UK, EARSEL. pp. 56–57.

Barnsley, M.J., Settle, J.J., Cutter, M.A., Lobb, D.R., Teston, F., 2004. The PROBA/CHRIS mission: a low-cost smallsat for hyperspectral multiangle observations of the earth surface and atmosphere. IEEE Trans. Geosci. Remote Sens. 42 (7), 1512–1520.

Battaglia, S., 2004. Variations in the chemical composition of illite from five geothermal fields: a possible geothermometer. Clay Miner. 39 (4), 501–510.

Bedini, E., van der Meer, F., van Ruitenbeek, F., 2009. Use of HyMap imaging spectrometer data to map mineralogy in the Rodalquilar caldera, southeast Spain. Int. J. Remote Sens. 30 (2), 327–348.

Bedini, E., 2009. Mapping lithology of the Sarfartoq carbonatite complex, southern West Greenland, using HyMap imaging spectrometer data. Remote Sens. Environ. 113 (6), 1208–1219.

Bishop, C.A., Liu, J.G., Mason, P.J., 2011. Hyperspectral remote sensing for mineral exploration in Pulang, Yunnan Province, China. Int. J. Remote Sens. 32 (9), 2409–2426.

Boardman, J., 1994. Geometric mixture analysis of imaging spectrometry data. International Geoscience and Remote Sensing Symposium, vol. 4, 2369–2371.

Bolin, B.J., Moon, T.S., 2003. Sulfide detection in drill core from the stillwater complex using visible/near-infrared imaging spectroscopy. Geophysics 68 (5), 1561–1568.

Brando, V.E., Dekker, A.G., 2003. Satellite hyperspectral remote sensing for estimating estuarine and coastal water quality. IEEE Trans. Geosci. Remote Sens. 41 (6), 1378–1387.

Buckingham, R., Staenz, K., 2008. Review of current and planned civilian space hyperspectral sensors for EO. Can. J. Remote Sens. 34, S187–S197.

Buckley, S.J., Kurz, T.H., Howell, J.A., Schneider, D., 2013. Terrestrial lidar and hyperspectral data fusion products for geological outcrop analysis. Comput. Geosci. 54, 249–258.

Calin, M.A., Parasca, S.V., Savastru, D., Manea, D., 2014. Hyperspectral imaging in the medical field: present and future. Appl. Spectrosc. Rev. 49 (6), 435–447.

Capobianco, G., Prestileo, F., Serranti, S., Bonifazi, G., 2015. Hyperspectral imaging-based approach for the in-situ characterization of ancient Roman wall paintings. Periodico Di Mineralogia 84 (3A), 407–418.

Carranza, E.J.M., van Ruitenbeek, F.J.A., Hecker, C., van der Meijde, M., van der Meer, F.D., 2008. Knowledge-guided data-driven evidential belief modeling of mineral prospectivity in Cabo de Gata, SE Spain. Int. J. Appl. Earth Obs. Geoinf. 10 (13), 374–387.

Chang, C.I., Wu, C.C., Lo, C.S., Chang, M.L., 2010. Real-time simplex growing algorithms for hyperspectral endmember extraction. IEEE Trans. Geosci. Remote Sens. 48 (4), 1834–1850.

Clark, R.N., Roush, T.L., 1984. Reflectance spectroscopy – quantitative-analysis techniques for remote-sensing applications. J. Geophys. Res. 89 (NB7), 6329–6340.

Cooper, B.L., Salisbury, J.W., Killen, R.M., Potter, A.E., 2002. Midinfrared spectral features of rocks and their powders. J. Geophys. Res.-Planets 107 (E4).

Cudahy, T.J., Caccetta, M., Chia, J., Collings, S., Hewson, R.D., 2010. Towards global mapping of the earth's land surface composition. In: In: Kajiwara, K., Muramatsu, K., Soyama, N., Endo, T., Ono, A., Akatsuka, S. (Eds.), Networking the World with Remote Sensing, vol. 38. pp. 459–463.

Cudahy, T., 2016. Towards a seamless, scalable world of 3D mineralogy. In: 2016 IEEE International Geoscience and Remote Sensing Symposium. New York, IEEE. pp. 5406–5409.

Debba, P., Carranza, E.J.M., van der Meer, F.D., Stein, A., 2006. Abundance estimation of spectrally similar minerals by using derivative spectra in simulated annealing. IEEE Trans. Geosci. Remote Sens. 44 (12), 3649–3658.

Debba, P., Carranza, E.J.M., Stein, A., van der Meer, F.D., 2009. Deriving optimal exploration target zones on mineral prospectivity maps. Math. Geosci. 41 (4), 421–446.

Duke, E.F., 1994. Near-infrared spectra of muscovite, Tschermak substitution, and metamorphic reaction progress – implications for remote-sensing. Geology 22 (7), 621–624.

Ferrier, G., Wadge, G., 1996. The application of imaging spectrometry data to mapping alteration zones associated with gold mineralization in southern Spain. Int. J. Remote Sens. 17 (2), 331–350.

Ferrier, G., White, K., Griffiths, G., Bryant, R., Stefouli, M., 2002. The mapping of hydrothermal alteration zones on the island of Lesvos, Greece using an integrated remote sensing dataset. Int. J. Remote Sens. 23 (2), 341–356.

Ferrier, G., Hudson-Edwards, K.A., Pope, R.J., 2009. Characterisation of the environmental impact of the Rodalquilar mine, Spain by ground-based reflectance spectroscopy. J. Geochem. Explor. 100 (1), 11–19.

Goetz, A.F.H., 2009. Three decades of hyperspectral remote sensing of the Earth: a personal view. Remote Sens. Environ. 113, S5–S16.

Grebby, S., Cunningham, D., Tansey, K., Naden, J., 2014. The impact of vegetation on lithological mapping using airborne multispectral data: a case study for the north troodos region, cyprus. Remote Sens. 6 (11), 10860–10887.

Green, D., Schodlok, M., 2016. Characterisation of carbonate minerals from hyperspectral

TIR scanning using features at 14 000 and 11 300 nm. Aust. J. Earth Sci. 63 (8), 951–957.
Hewson, R.D., Cudahy, T.J., Mizuhiko, S., Ueda, K., Mauger, A., 2005. Seamless geological map generation using ASTER in the Broken Hill-Curnamona province of Australia. Remote Sens. Environ. 9 (1), 59–172.
Hewson, R.D., Cudahy, T.J., Caccetta, M., Rodger, A., Jones, M., Ong, C., Ieee, 2009. Advances in hyperspectral processing for province- and continental-wide mineral mapping, 2009. IEEE International Geoscience and Remote Sensing Symposium, vol. 1–5, 3081–3084.
Jakob, S., Zimmermann, R., Gloaguen, R., 2017. The need for accurate geometric and radiometric corrections of drone-borne hyperspectral data for mineral exploration: MEPHySToA toolbox for pre-processing drone-borne hyperspectral data. Remote Sens. 9 (1).
Keshava, N., Mustard, J.F., 2002. Spectral unmixing. IEEE Signal Process Mag. 19 (1), 44–57.
Kokaly, R.F., Clark, R.N., 1999. Spectroscopic determination of leaf biochemistry using band-depth analysis of absorption features and stepwise multiple linear regression. Remote Sens. Environ. 67 (3), 267–287.
Kokaly, R.F., Couvillion, B.R., Holloway, J.M., Roberts, D.A., Ustin, S.L., Peterson, S.H., Khanna, S., Piazza, S.C., 2013. Spectroscopic remote sensing of the distribution and persistence of oil from the Deepwater Horizon spill in Barataria Bay marshes. Remote Sens. Environ. 129, 210–230.
Kopačková, V., Koucká, L., 2017. Integration of absorption feature information within visible to longwave infrared spectral ranges: demonstrating a synergy effect for more complex mineral mapping. Remote Sens. 9 (10), 1006. http://dx.doi.org/10.3390/rs9101006.
Kopacková, V., Koucká, L., 2014a. Mineral mapping based on automatic detection of multiple absorption features. EARSEL eProc. 13 (S1), 95–99.
Kopacková, V., Koucká, L., 2014b. QUANTOOLS: New Tools for Mineral Mapping Using High Spectral Resolution Data, 2014 GRSG AGM – 25 Years of Geological Remote Sensing. U.K Geological Society of London, London.
Kopacková, V., 2015. A New Version of QUANTOOLS, the Spectral Tools for Mineral Mapping, 2015 GRSG AGM – Challenges in Geological Remote Sensing. Geological Society of London, Frascati, Italy.
Kopackova, V., 2014. Using multiple spectral feature analysis for quantitative pH mapping in a mining environment. Int. J. Appl. Earth Obs. Geoinf. 28, 28–42.
Kruse, F.A., Perry, S.L., 2013. Mineral mapping using simulated worldview-3 short-wave-infrared imagery. Remote Sens. 5 (6), 2688–2703.
Kruse, F.A., Lefkoff, A.B., Boardman, J.W., Heidebrecht, K.B., Shapiro, A.T., Barloon, P.J., Goetz, A.F.H., 1993. The spectral image-processing system (SIPS) – interactive visualisation and analysis of imaging spectrometer data. Remote Sens. Environ. 44 (2–3), 145–163.
Kruse, F.A., 2015. Integrated visible and near-infrared, shortwave infrared, and longwave infrared full-range hyperspectral data analysis for geologic mapping. J. Appl. Remote Sens. 9.
Kumar, A.S., Keerthi, V., Manjunath, A.S., van der Werff, H., van der Meer, F., 2010. Hyperspectral image classification by a variable interval spectral average and spectral curve matching combined algorithm. Int. J. Appl. Earth Obs. Geoinf. 12 (4), 261–269.
Kurz, T.H., Buckley, S.J., 2016. A review of hyperspectral imaging in close range applications. In: In: Halounova, L., Safar, V., Remondino, F., Hodac, J., Pavelka, K., Shortis, M., Rinaudo, F., Scaioni, M., Boehm, J., RiekeZapp, D. (Eds.), XXIII ISPRS Congress, Commission V, vol. 41. pp. 865–870.
Lammoglia, T., de Souza, C.R., 2011. Spectroscopic characterization of oils yielded from Brazilian offshore basins: potential applications of remote sensing. Remote Sens. Environ. 115 (10), 2525–2535.
Lee, C.M., Cable, M.L., Hook, S.J., Green, R.O., Ustin, S.L., Mandl, D.J., Middleton, E.M., 2015. An introduction to the NASA Hyperspectral InfraRed Imager (HyspIRI) mission and preparatory activities. Remote Sens. Environ. 167, 6–19.
Lu, G.L., Fei, B.W., 2014. Medical hyperspectral imaging: a review. J. Biomed. Opt. 19 (1).
Mainali, D., Li, J., Yehl, P., Chetwyn, N., 2014. Development of a comprehensive near infrared spectroscopy calibration model for rapid measurements of moisture content in multiple pharmaceutical products. J. Pharm. Biom. Anal. 95, 169–175.
Mathieu, M., Roy, R., Launeau, P., Cathelineau, M., Quirt, D., 2017. Alteration mapping on drill cores using a HySpex SWIR-320 m hyperspectral camera: application to the exploration of an unconformity-related uranium deposit (Saskatchewan, Canada). J. Geochem. Explor. 172, 71–88.
Mielke, C., Boesche, N.K., Rogass, C., Kaufmann, H., Gauert, C., 2015. New geometric hull continuum removal algorithm for automatic absorption band detection from spectroscopic data. Remote Sens. Lett. 6 (2), 97–105.
Mielke, C., Rogass, C., Boesche, N., Segl, K., Altenberger, U., 2016. EnGeoMAP 2.0-automated hyperspectral mineral identification for the german EnMAP space mission. Remote Sens. 8 (2).
Montero, I.C., Brimhall, G.H., Alpers, C.N., Swayze, G.A., 2005. Characterization of waste rock associated with acid drainage at the Penn Mine, California by ground-based visible to short-wave infrared reflectance spectroscopy assisted by digital mapping. Chem. Geol. 215 (1–4), 453–472.
Murphy, R.J., Monteiro, S.T., Schneider, S., 2012. Evaluating classification techniques for mapping vertical geology using field-based hyperspectral sensors. IEEE Trans. Geosci. Remote Sens. 50 (8), 3066–3080.
Neville, R.A., Levesque, J., Staenz, K., Nadeau, C., Hauff, P., Borstad, G.A., 2003. Spectral unmixing of hyperspectral imagery for mineral exploration: comparison of results from SFSI and AVIRIS. Can. J. Remote Sens. 29 (1), 99–110.
Notesco, G., Kopackova, V., Rojik, P., Schwartz, G., Livne, I., Ben Dor, E., 2014. Mineral classification of land surface using multispectral lwir and hyperspectral swir remote-sensing data. A case study over the Sokolov lignite open-pit mines, the Czech Republic. Remote Sens. 6 (8), 7005–7025.
Pearlman, J.S., Barry, P.S., Segal, C.C., Shepanski, J., Beiso, D., Carman, S.L., 2003. Hyperion, a space-based imaging spectrometer. IEEE Trans. Geosci. Remote Sens. 41 (6), 1160–1173.
Pontius, R.G., Millones, M., 2011. Death to Kappa: birth of quantity disagreement and allocation disagreement for accuracy assessment. Int. J. Remote Sens. 32 (15), 4407–4429.
Richter, R., Schlapfer, D., 2002. Geo-atmospheric processing of airborne imaging spectrometry data. Part 2: atmospheric/topographic correction. Int. J. Remote Sens. 23 (13), 2631–2649.
Rodger, A., Laukamp, C., Haest, M., Cudahy, T., 2012. A simple quadratic method of absorption feature wavelength estimation in continuum removed spectra. Remote Sens. Environ. 118, 273–283.
Rytuba, J.J., Arribas, A., Cunningham, C.G., McKee, E.H., Podwysocki, M.H., Smith, J.G., Kelly, W.C., 1990. Mineralized and unmineralized calderas in Spain. 2. Evolution of the Rodalquilar caldera complex and associated gold-alunite deposits. Miner. Deposita 25, S29–S35.
Schlapfer, D., Richter, R., 2002. Geo-atmospheric processing of airborne imaging spectrometry data. Part 1: parametric orthorectification. Int. J. Remote Sens. 23 (13), 2609–2630.
Settle, J.J., Drake, N.A., 1993. Linear mixing and the estimation of ground cover proportions. Int. J. Remote Sens. 14 (6), 1159–1177.
Shrestha, D.P., Margate, D.E., van der Meer, F., Anh, H.V., 2005. Analysis and classification of hyperspectral data for mapping land degradation: an application in southern Spain. Int. J. Appl. Earth Obs. Geoinf. 7 (2), 85–96.
Snyder, C.J., Khan, S.D., Bhattacharya, J.P., Glennie, C., Seepersad, D., 2016. Thin-bedded reservoir analogs in an ancient delta using terrestrial laser scanner and high-resolution ground-based hyperspectral cameras. Sediment. Geol. 342, 154–164.
Staenz, K., Held, A., 2012. Summary of current and future terrestrial civilian hyperspectral spaceborne systems. 2012 IEEE International Geoscience and Remote Sensing Symposium 123–126.
Stuffler, T., Kaufmann, C., Hofer, S., Forster, K.P., Schreier, G., Mueller, A., Eckardt, A., Bach, H., Penne, B., Benz, U., Haydn, R., 2007. The EnMAP hyperspectral imager – an advanced optical payload for future applications in Earth observation programmes. Acta Astronaut. 61 (1–6), 115–120.
Tangestani, M.H., Mazhari, N., Agar, B., Moore, F., 2008. Evaluating advanced space-borne thermal emission and reflection radiometer (ASTER) data for alteration zone enhancement in a semi-arid area, northern Shahr-e-Babak, SE Iran. Int. J. Remote Sens. 29 (10), 2833–2850.
Tappert, M.C., Rivard, B., Fulop, A., Rogge, D., Feng, J., Tappert, R., Stalder, R., 2015. Characterizing kimberlite dilution by crustal rocks at the snap lake diamond mine (Northwest Territories, Canada) using SWIR (1.90–2.36 mu m) and LWIR (8.1–11.1 mu m) hyperspectral imagery collected from drill core. Econ. Geol. 110 (6), 1375–1387.
Van Ruitenbeek, F.J.A., Cudahy, T., Hale, M., van der Meer, F.D., 2005. Tracing fluid pathways in fossil hydrothermal systems with near-infrared spectroscopy. Geology 33 (7), 597–600.
Van Ruitenbeek, F.J.A., Debba, P., van der Meer, F.D., Cudahy, T., van der Meijde, M., Hale, M., 2006. Mapping white micas and their absorption wavelengths using hyperspectral band ratios. Remote Sens. Environ. 102 (3–4), 211–222.
Winter, M.E., 1999. N-FINDR: an algorithm for fast autonomous spectral end-member determination in hyperspectral data. In: In: Descour, M.R., Shen, S.S. (Eds.), Imaging Spectrometry V, vol. 3753. Spie-Int Soc Optical Engineering, Bellingham, pp. 266–275.
Youngentob, K.N., Renzullo, L.J., Held, A.A., Jia, X.P., Lindenmayer, D.B., Foley, W.J., 2012. Using imaging spectroscopy to estimate integrated measures of foliage nutritional quality. Methods Ecol. Evol. 3 (2), 416–426.
Zortea, M., Plaza, A., 2009. A quantitative and comparative analysis of different implementations of N-FINDR: a fast endmember extraction algorithm. IEEE Geosci. Remote Sens. Lett. 6 (4), 787–791.
da Silva, V.H., Goncalves, J.L., Vasconcelos, F.V.C., Pimentel, M.F., Pereira, C.F., 2015. Quantitative analysis of mebendazole polymorphs in pharmaceutical raw materials using near-infrared spectroscopy. J. Pharm. Biom. Anal. 115, 587–593.
van Ruitenbeek, F.J.A., Bakker, W.H., van der Werff, H.M.A., Zegers, T.E., Oosthoek, J.H.P., Omer, Z.A., Marsh, S.H., van der Meer, F.D., 2014. Mapping the wavelength position of deepest absorption features to explore mineral diversity in hyperspectral images. Planet. Space Sci. 101, 108–117.
van der Meer, F.D., van der Werff, H.M.A., van Ruitenbeek, F.J.A., Hecker, C.A., Bakker, W.H., Noomen, M.F., van der Meijde, M., Carranza, E.J.M., de Smeth, J.B., Woldai, T., 2012. Multi- and hyperspectral geologic remote sensing: a review. Int. J. Appl. Earth Obs. Geoinf. 14 (1), 112–128.
van der Meer, F., 1996. Spectral mixture modelling and spectral stratigraphy in carbonate lithofacies mapping. ISPRS J. Photogramm. Remote Sens. 51 (3), 150–162.
van der Meer, F., 2000. Spectral curve shape matching with a continuum removed CCSM algorithm. Int. J. Remote Sens. 21 (16), 3179–31852.
van der Meer, F., 2006. The effectiveness of spectral similarity measures for the analysis of hyperspectral imagery. Int. J. Appl. Earth Obs. Geoinf. 8 (1), 3–17.
van der Werff, H., van der Meer, F., 2015. Sentinel-2 for mapping iron absorption feature parameters. Remote Sens. 7 (10), 12635–12653.